Perovskite light-emitting diodes based on solution-processed self-organized multiple quantum wells

Nana Wang[1†], Lu Cheng[1†], Rui Ge[1†], Shuting Zhang[1], Yanfeng Miao[1], Wei Zou[1], Chang Yi[1], Yan Sun[1], Yu Cao[1], Rong Yang[1], Yingqiang Wei[1], Qiang Guo[1], You Ke[1], Maotao Yu[1], Yizheng Jin[2], Yang Liu[3], Qingqing Ding[4], Dawei Di[5], Le Yang[5], Guichuan Xing[1], He Tian[4], Chuanhong Jin[4], Feng Gao[6], Richard H. Friend[5], Jianpu Wang[1*] and Wei Huang[1,7*]

Organometal halide perovskites can be processed from solutions at low temperatures to form crystalline direct-bandgap semiconductors with promising optoelectronic properties[1–5]. However, the efficiency of their electroluminescence is limited by non-radiative recombination, which is associated with defects and leakage current due to incomplete surface coverage[6–9]. Here we demonstrate a solution-processed perovskite light-emitting diode (LED) based on self-organized multiple quantum wells (MQWs) with excellent film morphologies. The MQW-based LED exhibits a very high external quantum efficiency of up to 11.7%, good stability and exceptional high-power performance with an energy conversion efficiency of 5.5% at a current density of 100 mA cm^{-2}. This outstanding performance arises because the lower bandgap regions that generate electroluminescence are effectively confined by perovskite MQWs with higher energy gaps, resulting in very efficient radiative decay. Surprisingly, there is no evidence that the large interfacial areas between different bandgap regions cause luminescence quenching.

Recently, high-efficiency photovoltaic devices based on three-dimensional (3D) organometal halide perovskites, such as $CH_3NH_3PbI_3$ and $NH_2CH = NH_2PbI_3$ (FAPbI$_3$), have been demonstrated[3–5]. Hybrid 3D perovskites exhibit high photoluminescence quantum efficiencies (PLQEs) and good charge mobilities, making them attractive for electroluminescence (EL) applications[2,8,9]. Encouraging performance metrics of LEDs based on 3D perovskites, such as low turn-on voltages and external quantum efficiencies (EQEs) of up to 3.5% at high current densities, have been demonstrated[9]. However, the EL quantum efficiency is far below the limit predicated by the approximately 70% PLQE of the 3D perovskites, mainly due to the existence of current losses that are caused by incomplete surface coverage of the perovskite films and the fact that the high PLQE can only be obtained at high excitations[8,9]. By using thick (>300 nm) perovskite films, LEDs with over 8% EQE[10] were obtained, but the turn-on voltage is high and the power efficiency is low, possibly a result of the thick perovskite layer used. To further enhance the performance of 3D perovskite-based LEDs, it is essential to obtain perovskite thin films with both complete surface coverage and high PLQE[8–10]. Moreover, device stability,

which was proven to be a vital issue in organic–inorganic halide perovskite-based photovoltaics[11], has not been addressed in perovskite LEDs.

The 3D perovskites are actually an extreme case of layered organometal halide perovskites with a general formula of $L_2(SMX_3)_{n-1}MX_4$, where M, X, L, and S are a divalent metal cation, a halide and organic cations with long and short chains, respectively (Fig. 1a)[12–14]. Here n is the number of semiconducting MX_4 monolayer sheets within the two organic insulating layers (cation L), with $n = \infty$ corresponding to the structure of a 3D perovskite SMX_3. With smaller numbers of MX_4 layers, quantum confinement effects (such as increases in the bandgap and exciton energies) become important[6,15]. In consequence, the layered perovskites naturally form QW structures. At the opposite extreme, when $n = 1$, the layered perovskites form a monolayer structure of a 2D perovskite L_2MX_4. The 2D L_2MX_4 perovskites generally have good film-formation properties[13]. Nevertheless, the PLQEs of the 2D perovskites are low at room temperature owing to fast exciton quenching rates[6,7]. LEDs based on the 2D perovskites have been attempted, but the devices are either very low in efficiency or only operational at cryogenic temperatures[16–18]. Here we demonstrate very efficient (up to 11.7% EQE) and high-brightness EL achievable at room temperature by using solution-processed perovskite MQWs with an energy cascade, which can combine the advantages of 2D and 3D perovskites. We note that a relevant perovskite LED work[19] that shows a peak EQE of 8.8% has been published online during the revision of this Letter.

A precursor solution of 1-naphthylmethylamine iodide (NMAI), formamidinium iodide (FAI) and PbI$_2$ with a molar ratio of 2:1:2 dissolved in N,N-dimethylformamide (DMF) was used to deposit perovskite films (see Methods for details), hereafter referred to as NFPI$_7$ films. Atomic force microscopy (AFM) measurements show that the NFPI$_7$ film has a smooth and uniform surface coverage (Fig. 1b). The root-mean-square (r.m.s.) roughness of the NFPI$_7$ film (2.6 nm) is comparable to that of the 2D (NMA)$_2$PbI$_4$ ($n = 1$) perovskite film (1.4 nm) and much lower than that of the 3D FAPbI$_3$ ($n = \infty$) perovskite film (18.8 nm; Supplementary Fig. 1).

We study the optical properties of the NFPI$_7$ films. Because of the quantum confinement effects, the absorption and emission features
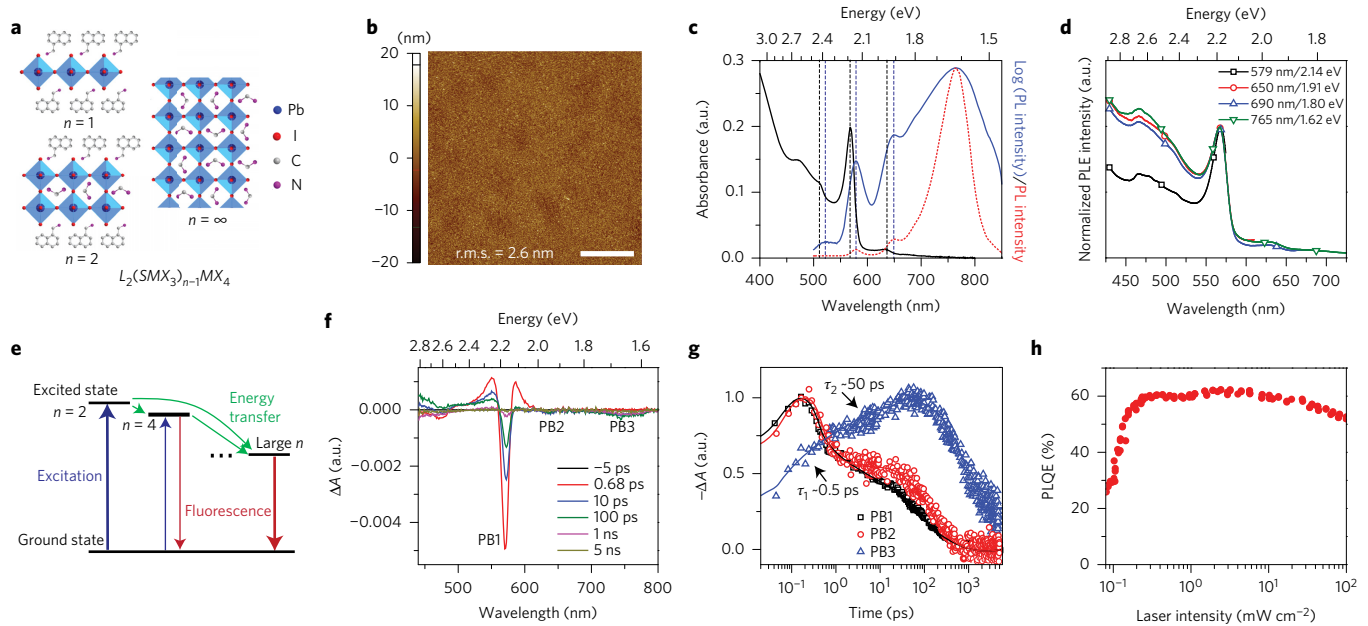
Figure 1 | Perovskite MQW films. a, Schematic representation of the structures of the layered lead halide perovskites with $n = 1$, $n = 2$ and $n = \infty$. **b**, An AFM height image of the NFPI$_7$ MQW film (scale bar, 5 μm). **c**, Absorption and PL (445 nm excitation) spectra of the NFPI$_7$ MQW film deposited onto quartz substrates. The PL spectrum is plotted in log scale (blue curve) and linear scale (red curve). The three pairs of the dashed lines (from left to right) correspond to the absorption (black) and PL (red) peaks from the QWs with $n = 1$, 2 and 4, respectively. **d**, PL excitation spectra of the NFPI$_7$ MQW film at various emission energies. **e**, Schematic of cascade energy transfer in MQWs. Excitation energy is transferred downstream from smaller-n QWs to larger-n QWs, and the emission is mainly from larger-n QWs. **f**, Photo-induced changes in transient absorption spectra (ΔA) of the MQWs at selected probe delay times, which shows photobleaching at PB1 (2.18 eV), PB2 (1.95 eV) and PB3 (1.64 eV). **g**, Normalized bleaching kinetics at 2.18 eV, 1.95 eV and 1.64 eV for the MQWs following excitation at 400 nm (1 KHz, 50 fs, ~0.4 μJ cm^{-2}), which shows a fast exciton localization time (τ_1) and a relatively slow exciton localization time (τ_2). **h**, Excitation-intensity-dependent PLQE of the NFPI$_7$ MQW film.

of the layered perovskites depend on the value of n[6,15]. Previous studies on PbI$_4$-based perovskites showed that the absorption peaks at around 2.4, 2.2, 2.0 and 1.9 eV correspond to excitonic absorption of QWs with $n = 1$, 2, 3 and 4 respectively[6,20,21]. Our results confirm that the (NMA)$_2$PbI$_4$ perovskite film, that is, the $n = 1$ QW film, presents a strong peak at 2.43 eV (Supplementary Fig. 2). The absorption spectrum of the NFPI$_7$ film shows a strong exciton absorption peak at 2.18 eV (Fig. 1c), indicating that the major component of the perovskite film is (NMA)$_2$(FAPbI$_3$) PbI$_4$, that is, the $n = 2$ QWs. The shoulders at 2.43 eV and 1.95 eV suggest the existence of small fractions of $n = 1$ and $n = 4$ perovskite QWs respectively, while the absorption peak of the $n = 3$ QWs at around 2.0 eV may be hidden by the absorption tail of the $n = 2$ QWs. Optical features corresponding to QWs with higher n values are not evident in the absorption spectrum. They become visible in the PL spectrum, as shown by the dominating peak at 1.62 eV. This emission is blueshifted by around 40 nm compared with that of bulk 3D ($n = \infty$) FAPbI$_3$ perovskite (1.54 eV, Supplementary Fig. 2). The PL spectrum on a semi-log scale reveals several weak emission peaks at 2.38 eV, 2.14 eV and 1.91 eV. With the absorption and emission spectra plotted in the same panel (Fig. 1c), it can be seen that absorption and emission peaks for $n \leq 4$ QWs correspond very well to each other. We point out that although $n = 2$ QWs give the strongest absorption peak in the NFPI$_7$ films, the emission from them is very weak.

The investigations above suggest that our NFPI$_7$ film is an ensemble of self-organized MQWs with different exciton energies. The absorption and PL measurements clearly demonstrate energy transfer from QWs with large exciton energies to QWs with lower exciton energies. PL excitation measurements on the NFPI$_7$ film show that different emissions share a strong excitation peak at 2.18 eV (Fig. 1d), showing that there is energy transfer from $n = 2$ QWs to the lower-energy emissions. For the 765 nm/1.62 eV

emission, the PL excitation spectrum also reveals weak contributions from QWs with $n > 2$. The observation of weak emission from the $n = 1$, $n = 2$ and $n = 4$ QWs demonstrates that the energy migration is not complete. The cascade energy transfer of photon excitation in the perovskite MQWs is illustrated in Fig. 1e.

Transient absorption measurements further show that the energy transfer between the perovskite QWs is an ultrafast process (Fig. 1f). With 400 nm excitation, the excitons are primarily formed in the $n = 2$ QWs. This manifests as a fast build-up of the photobleaching (PB) at the exciton absorption peak (2.18 eV) of the $n = 2$ QWs. The evolution of the transient absorption spectra shows that the excitons reach the large-n QWs (around 1.64 eV) after some time delay. The PB of the large-n QWs resonance grows over time. Time traces at selected probe wavelengths are shown in Fig. 1g. The PB of $n = 2$ QWs (approximately 2.18 eV) shows an ultrafast dominant decay with a time constant of around 0.5 ps. This decay time is closely matched with the fast PB formation time of the large-n QWs (about 1.64 eV). This result indicates that a substantial portion of the photogenerated excitons from $n = 2$ QWs will be localized to large-n QWs within 0.5 ps. Subsequently, a slower decay of the PB of $n = 2$ QWs also matches well with the relative slower formation of the large-n QWs PB. This relatively slower exciton localization time is fitted to be about 50 ps.

The rapid energy transfer process in the perovskite MQWs can essentially avoid the exciton quenching effect presented in previously reported 2D perovskites[6,7]. Figure 1h shows the light-intensity-dependent PLQE of the NFPI$_7$ film under a 445 nm continuous wave laser excitation. The high PLQE of up to 60% suggests that the photogenerated excitons in small-n QWs can be energy transferred to the large-n QWs with superior emission properties, allowing efficient radiative recombination. Remarkably, the MQW films present high PLQEs at an excitation as low as about 0.3 mW cm^{-2}. This feature is very different from that of the bulk 3D perovskite
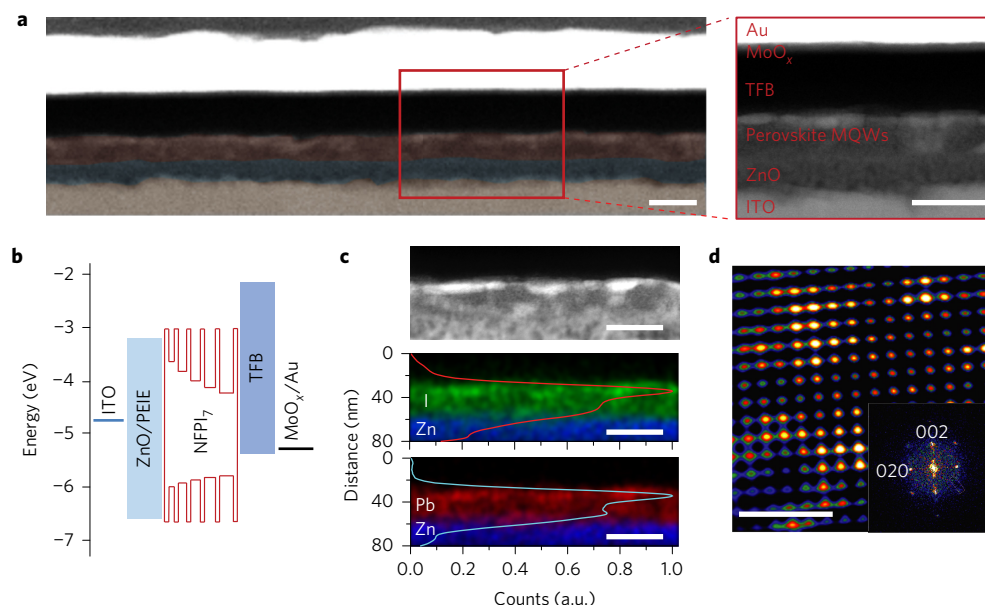
Figure 2 | Device structure of the NFPI₇ perovskite MQW LED. a, A cross-sectional STEM image (scale bar, 50 nm) showing the device architecture: ITO/PEIE modified ZnO (around 20 nm)/NFPI₇ (around 30 nm)/TFB (around 40 nm)/MoO$_x$ (around 7 nm)/Au. The different layers in the left panel have been tinted. **b**, Flat-band energy level diagram. Except for NFPI₇, the energy level values of the other layers were taken from the literature[9]. **c**, EDX mapping. Colour-mixed EDX mapping images (scale bar, 50 nm) present the element distribution of Pb, I and Zn. The normalized EDX count distribution of Pb and I across the perovskite layer are also presented. **d**, FFT-filtered HRTEM image (scale bar, 2 nm) and FFT analyses (inset) of a perovskite crystal close to the TFB/perovskite interface show that this crystal has a cubic structure similar to that of the 3D α-FAPbI₃[22].

films, which have high PLQEs only at very high excitations, over 500 mW cm⁻² , for example[2] (Supplementary Fig. 3). The high PLQEs of the perovskite emitters can be obtained when the non-radiative decay centres are filled by excitations[9]. In our MQW perovskite films, the exciton decay in large-n QWs is much slower (Supplementary Fig. 4) than the energy transfer process. As a result, most of the photogenerated excitons formed are concentrated in the small space of the large-n QWs, which can substantially increase the local exciton density in the emissive large-n QWs. Furthermore, the QW structure can effectively confine the excitons and reduce the exciton diffusion lengths, which can decrease the probability of exciton-defect quenching.

The desirable film morphology and optical properties of the NFPI₇ film encourage us to fabricate LEDs based on perovskite MQWs. Figure 2a shows the cross-sectional view of a device with a multi-layer structure of indium tin oxide (ITO)/polyethylenimine ethoxylated (PEIE)-modified zinc oxide (ZnO, around 20 nm)/ perovskite MQWs (around 30 nm)/poly(9,9-dioctyl-fluorene-co-N-(4-butylphenyl)diphenylamine) (TFB, approximately 40 nm)/molybdenum oxide (MoO$_x$, around 7 nm)/gold (Au, about 60 nm). All layers, apart from the MoO$_x$/Au electrode, were deposited from solutions. The flat-band energy levels of the layers are indicated in Fig. 2b, and the energy level values for NFPI₇ film were estimated by ultraviolet photoelectron spectroscopy (UPS) (Supplementary Fig. 5) and optical measurements. The PEIE-modified ZnO and TFB layers are employed as electron-transporting interlayers and hole-transporting interlayers respectively. The MoO$_x$/Au bilayers and ITO are selected as the top electrodes and bottom electrodes, respectively.

A cross-sectional sample of the NFPI₇ device was analysed by an aberration-corrected scanning transmission electron microscope (STEM). A low-magnification high-angle annular dark-field (HAADF) image (Fig. 2a) illustrates the multiple layers of materials with distinct contrast. The approximately 30 nm thick perovskite layer is smooth and pin-hole free (determined by STEM inspections), agreeing well with the AFM results, which indicates that the NFPI₇ film has a low surface roughness. Zoomed-in observations

show that the perovskite layer exhibits contrasts, with the majority of brighter regions close to the perovskite/TFB interface. We propose that the contrasts in the perovskite layer reflect the spatial distributions of QWs with different n values. Perovskite QWs with larger n values accommodate more PbI₄ units per volume, thereby resulting in a higher intensity of large-angle elastic scattering and in consequence appear brighter in the HAADF imaging. In other words, the majority of large-n QWs are located in the regions close to the perovskite/TFB interface. This deduction is supported by both energy-dispersive X-ray spectroscopy (EDX) elemental mapping and high-resolution transmission electron microscopy (HRTEM) results (Fig. 2c,d). EDX maps show stronger signals of both lead and iodide in the brighter regions. The distribution of lead and iodide across the perovskite layer suggests that the large-n QWs and small-n QWs locate at the interfaces between perovskite/TFB and perovskite/ZnO, respectively. The large-n QW region is much narrower than the small-n QW region, which presumably is the $n = 2$ QWs, and a gradually graded or mixed QW region is in between. HRTEM and the corresponding fast Fourier transformation (FFT) analyses (Fig. 2d and Supplementary Fig. 6) show that the perovskite crystals close to the perovskite/TFB interface share the same cubic structure as the 3D α-FAPbI₃[22].

Figure 3a shows the EL spectra of devices based on NFPI₇ MQW films (see Supplementary Fig. 7 for the characterization set-up). The EL emission peak at the near-infrared (NIR), 786 nm/1.58 eV, is blueshifted by around 20 nm compared with the EL from bulk 3D FAPbI₃ perovskites (Supplementary Fig. 8). The shapes of the EL spectra do not change at different bias voltages (Supplementary Fig. 9). The NFPI₇-MQW LED turns on at a low voltage of 1.5 V (Fig. 3b). The current density and radiance rise rapidly by several orders of magnitude after turn-on, implying excellent charge injection and transport in the MQW LEDs. The EQE of the LED reaches 9.6% at 2.3 V with a current density of 15 mA cm⁻² (Fig. 3c). A high radiance of 55 W sr⁻¹ m⁻² is achieved at 3.6 V. The angular emission intensity of the device follows a Lambertian profile (Supplementary Fig. 10). The statistics from 67 devices
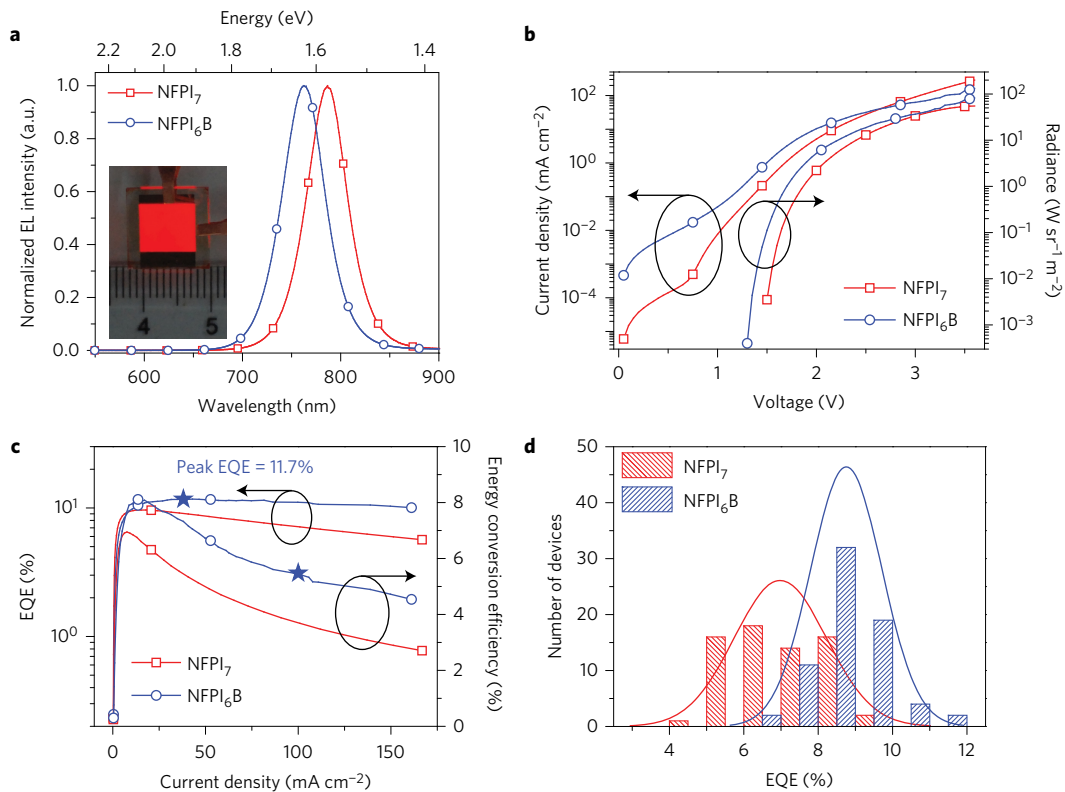
Figure 3 | Optoelectronic characteristics of the NFPI$_7$ and NFPI$_6$B perovskite MQW LEDs. a, EL spectra of the devices under 3 V. Inset, photograph of a 64 mm^2 NFPI$_6$B device. **b**, Dependence of the current density and radiance on the driving voltage. Radiances of 55 W sr^{-1} m^{-2} and 82 W sr^{-1} m^{-2} are obtained under 3.6 V for NFPI$_7$ and NFPI$_6$B devices, respectively. **c**, EQE and energy conversion efficiency versus current density. For the NFPI$_6$B MQW LED, a peak EQE of 11.7% is achieved at a current density of 38 mA cm^{-2} and an energy conversion efficiency of 5.5% is obtained at a current density of 100 mA cm^{-2}. **d**, Histograms of peak EQEs measured from 67 NFPI$_7$ and 70 NFPI$_6$B devices.

present an average EQE of 7.0% with a relative standard deviation of 18% (Fig. 3d), demonstrating good reproducibility of the NFPI$_7$-MQW LEDs.

We consider that the superior EL performance in the MQW LEDs is due to the confinement of injected charges in the large-n QWs which have excellent emission properties as shown by the PL measurements. In EL device operation, electrons and holes are injected into the perovskite layer and accumulated at the large-n QWs because of the cascade energy structure of the perovskite MQW films. In other words, the injected charges can directly recombine at the very thin layer of large-n QWs. This is consistent with our finding that the weak emissions at higher energies observed in the PL spectrum are absent in the EL measurements and the EL emission peak is slightly redshifted compared with the main PL peak (Fig. 3a and 1c). As shown by the PL investigations (Fig. 1h), the very thin layer of large-n QWs is highly emissive even at low excitations, which results in the high EL efficiency in our MQW perovskite LEDs. To fabricate high-efficiency perovskite LEDs, it is a challenge to obtain a large-n emissive thin layer with good coverage sandwiched between two non-quenching contacts with appropriate energy levels, while our MQW structure provides a simple alternative solution to it.

One of the advantages of perovskite materials is that the optoelectronics properties can be easily tuned by adjusting the composition. In perovskite solar cells, it has been shown that the device performance can be optimized by using mixed halogens, which improves the crystallinity of the perovskite film[23]. We show that it is possible to further enhance the efficiency of MQW LEDs by adopting a similar strategy (Supplementary Table 1). For example, we used a precursor solution of NMAI:FABr:PbI$_2$ with a molar ratio of 2:1:2 in DMF to deposit new perovskite MQW films

(abbreviated as NFPI$_6$B below). This NFPI$_6$B film has a PLQE of 67% (Supplementary Fig. 3), higher than that of the NFPI$_7$ film. The EL emission peak of LEDs based on the NFPI$_6$B film is shifted to 763 nm (Fig. 3a). The best-performing NFPI$_6$B LED turns on at 1.3 V. The EQE reaches 11.7% at 2.6 V with a current density of 38 mA cm^{-2}. A high radiance of around 82 W sr^{-1} m^{-2} is achieved at 3.6 V. These results represent the highest EQE for perovskite-based LEDs[9]. Remarkably, the device is highly efficient at high current densities. The energy conversion efficiency (wall-plug efficiency) of our NFPI$_6$B MQW LED is 5.5% at 100 mA cm^{-2}, which is more efficient than the state-of-the-art vacuum-deposited organic LEDs at this high current density (Supplementary Table 2)[24–26]. The EQE histogram for 70 NFPI$_6$B-MQW LEDs shows an average peak EQE of 8.8% and a small relative standard deviation of 11% (Fig. 3d). Owing to the good film uniformity, the size of the perovskite MQW LEDs can be easily scaled up by adopting the same device structure and fabrication process. Figure 3a also shows uniform and bright EL emission from an approximately 64 mm^2 NFPI$_6$B-MQW device with a peak EQE of 7.5%.

We can tune the EL across a wide range of the spectrum by further changing the halide compositions in precursor solutions. For example, the perovskite MQW LEDs can achieve narrow emission peaks at 736 nm, 685 nm, 664 nm, 611 nm or 518 nm, when the MQW films are produced by using precursor solutions with various ratios of Br to I (Fig. 4a). The various combinations of precursor solutions to produce the NFPI$_y$B$_{7-y}$ (y represents the fraction of I) films are provided in Supplementary Table 1. Figure 4b demonstrates bright and uniform emission from the green and red MQW LEDs, respectively. The symmetric and narrow emission peaks at 518 nm and 685 nm correspond to Commission Internationale de l'Eclairage (CIE) colour coordinates of (0.11, 0.74) and (0.72, 0.28)
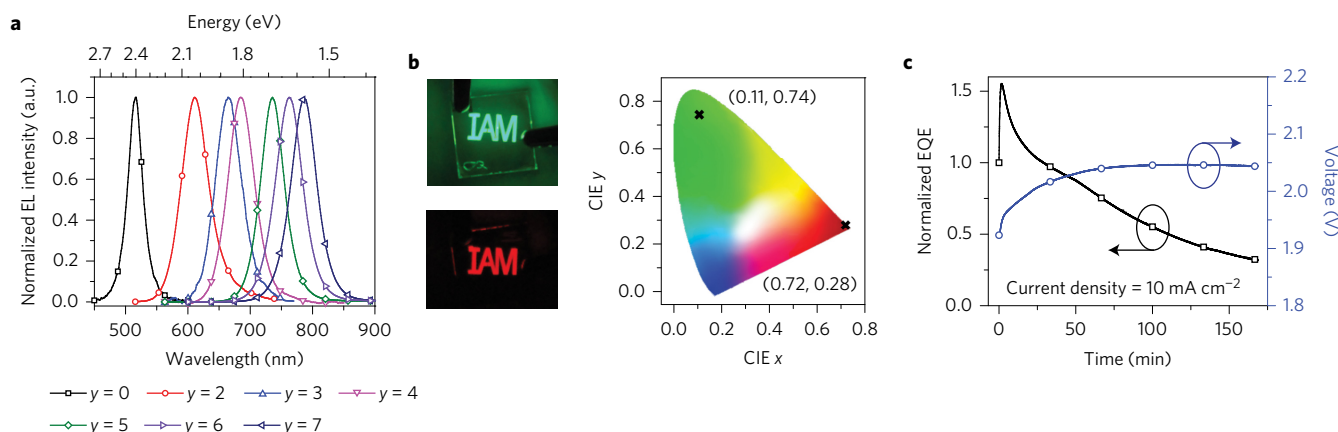
Figure 4 | EL colour tunability and device stability of the perovskite MQW LEDs. a, EL spectra of MQW LEDs based on the NFPI$_y$B$_{7-y}$ films, $y = 0, 2, 3, 4,$ 5, 6 and 7, respectively, which are processed using various combinations of precursor solutions of NMAI, FAI and PbI$_2$ (refer to Supplementary Table 1 for details). **b**, Photographs of green and red MQW LEDs with the logo of the IAM, and the corresponding CIE coordinates. **c**, Stability data for a NFPI$_7$ EL device tested at a constant current density of 10 mA cm^{-2}.

respectively, which are ideal for display applications. Supplementary Table 1 also summarizes the device performance of different-colour MQW LEDs with the same device structure. The performance of the visible LEDs is inferior to that of the NIR devices, which is probably due to either inefficient charge injection to the emitters with larger bandgap or lower PL efficiencies. By further optimizing the device structure and film processing, it is possible to enhance the MQW LED device performance in the visible range.

In addition to the remarkably high efficiency and readily colour tunability, the devices based on perovskite MQWs also demonstrate reasonably good stability. As shown in Fig. 4c, the EQE of the NFPI$_6$B devices dropped to half of the initial value after around 2 h under a constant current density of 10 mA cm^{-2}. This result shows that the stability of perovskite MQW LEDs is significantly improved (by two orders of magnitude) compared with LEDs based on the 3D perovskites produced in our laboratory, which can only survive for about 1 min under similar conditions (Supplementary Fig. 8). We believe that both the high power conversion efficiency of the LED and the stability of the perovskite QW films[21] contribute to the improved device lifetime.

The use of semiconductors with different bandgaps to engineer high-performance optoelectronic devices has of course been very effectively developed in group III–V semiconductors. This allows the control of the charge recombination sites and the luminescence wavelength, but requires very close control of the lattice parameter matching to avoid electronic defects that cause trapping and quenching. Our findings reveal that these mixed energy gap perovskite structures show no evidence of higher electronic defect densities than single-gap materials, in spite of the very high interfacial areas that must be present. This fact provides real promise for the further development of this class of materials, particularly for light emission.

Methods

Methods and any associated references are available in the online version of the paper.

References

1. Xing, G. et al. Low-temperature solution-processed wavelength-tunable perovskites for lasing. *Nat. Mater.* **13**, 476–480 (2014).
2. Deschler, F. et al. High photoluminescence efficiency and optically pumped lasing in solution-processed mixed halide perovskite semiconductors. *J. Phys. Chem. Lett.* **5**, 1421–1426 (2014).
3. Stranks, S. D. et al. Electron-hole diffusion lengths exceeding 1 micrometer in an organometal trihalide perovskite absorber. *Science* **342**, 341–344 (2013).
4. Burschka, J. et al. Sequential deposition as a route to high-performance perovskite-sensitized solar cells. *Nature* **499**, 316–319 (2013).
5. Yang, W. S. et al. High-performance photovoltaic perovskite layers fabricated through intramolecular exchange. *Science* **348**, 1234–1237 (2015).
6. Hong, X., Ishihara, T. & Nurmikko, A. V. Dielectric confinement effect on excitons in PbI$_4$-based layered semiconductors. *Phys. Rev. B* **45**, 6961–6964 (1992).
7. Gauthron, K. et al. Optical spectroscopy of two-dimensional layered (C$_6$H$_5$C$_2$H$_4$-NH$_3$)$_2$-PbI$_4$ perovskite. *Opt. Express* **18**, 5912–5919 (2010).
8. Tan, Z.-K. et al. Bright light-emitting diodes based on organometal halide perovskite. *Nat. Nanotech.* **9**, 687–692 (2014).
9. Wang, J. et al. Interfacial control toward efficient and low-voltage perovskite light-emitting diodes. *Adv. Mater.* **27**, 2311–2316 (2015).
10. Cho, H. et al. Overcoming the electroluminescence efficiency limitations of perovskite light-emitting diodes. *Science* **350**, 1222–1225 (2015).
11. Li, X. et al. Improved performance and stability of perovskite solar cells by crystal crosslinking with alkylphosphonic acid ω-ammonium chlorides. *Nat. Chem.* **7**, 703–711 (2015).
12. Calabrese, J. et al. Preparation and characterization of layered lead halide compounds. *J. Am. Chem. Soc.* **113**, 2328–2330 (1991).
13. Mitzi, D. B., Chondroudis, K. & Kagan, C. R. Organic–inorganic electronics. *IBM J. Res. Dev.* **45**, 29–45 (2001).
14. Tyagi, P., Arveson, S. M. & Tisdale, W. A. Colloidal organohalide perovskite nanoplatelets exhibiting quantum confinement. *J. Phys. Chem. Lett.* **6**, 1911–1916 (2015).
15. Ishihara, T. Optical-properties of PbI-based perovskite structures. *J. Lumin.* **60-61**, 269–274 (1994).
16. Hong, X., Ishihara, T. & Nurmikko, A. V. Photoconductivity and electroluminescence in lead iodide based natural quantum-well structures. *Solid State Commun.* **84**, 657–661 (1992).
17. Era, M., Morimoto, S., Tsutsui, T. & Saito, S. Organic–inorganic heterostructure electroluminescent device using a layered perovskite semiconductor (C$_6$H$_5$C$_2$H$_4$NH$_3$)$_2$PbI$_4$. *Appl. Phys. Lett.* **65**, 676–678 (1994).
18. Chondroudis, K. & Mitzi, D. B. Electroluminescence from an organic–inorganic perovskite incorporating a quaterthiophene dye within lead halide perovskite layers. *Chem. Mater.* **11**, 3028–3030 (1999).
19. Yuan, M. et al. Perovskite energy funnels for efficient light-emitting diodes. *Nat. Nanotech.* http://dx.doi.org/10.1038/nnano.2016.110 (2016).
20. Tanaka, K. & Kondo, T. Bandgap and exciton binding energies in lead-iodide-based natural quantum-well crystals. *Sci. Technol. Adv. Mater.* **4**, 599–604 (2003).
21. Smith, I. C., Hoke, E. T., Solis-Ibarra, D., McGehee, M. D. & Karunadasa, H. I. A layered hybrid perovskite solar-cell absorber with enhanced moisture stability. *Angew. Chem. Int. Ed.* **53**, 11232–11235 (2014).
22. Weller, M. T., Weber, O. J., Frost, J. M. & Walsh, A. Cubic perovskite structure of black formamidinium lead iodide, α-[HC(NH$_2$)$_2$]PbI$_3$, at 298 K. *J. Phys. Chem. Lett.* **6**, 3209–3212 (2015).
23. Jeon, N. J. et al. Compositional engineering of perovskite materials for high-performance solar cells. *Nature* **517**, 476–480 (2015).
24. Graham, K. R. et al. Extended conjugation platinum(II) porphyrins for use in near-infrared emitting organic light emitting diodes. *Chem. Mater.* **23**, 5305–5312 (2011).

25. Helander, M. G. *et al.* Chlorinated indium tin oxide electrodes with high
    work function for organic device compatibility. *Science* **332,**
    944–947 (2011).
26. Lai, C.-C. *et al. m*-indolocarbazole derivative as a universal host material
    for RGB and white phosphorescent OLEDs. *Adv. Funct. Mater.* **25,**
    5548–5556 (2015).

Author contributions

J.W. had the idea for and designed the experiments. J.W. and W.H. supervised the work.
L.C., R.G., N.W. and S.Z. carried out the device fabrication and characterizations. Y.M., Y.S.
and Y.C. conducted the optical measurements. W.Z. set up the testing systems and took part
in the optical measurements. C.Y. and Y.C. synthesized the NMAI/NMABr and measured
AFM. R.Y., Q.G., Y.K., M.Y., D.D. and L.Y. participated in the device fabrication and
characterizations. G.X. measured the transient absorption. Y.L., Q.D., H.T, C.J., Y.J. and
Y.W. carried out the HRTEM and STEM characterizations. J.W., N.W. and F.G. wrote the
first draft of the manuscript. Y.J., R.H.F. and W.H. participated in data analysis and
provided major revisions. All authors discussed the results and commented on
the manuscript.

Additional information

Supplementary information is available in the online version of the paper. Reprints and
permissions information is available online at www.nature.com/reprints. Correspondence and
requests for materials should be addressed to J.W. and W.H.

Competing financial interests

The authors declare no competing financial interests.

Methods

Synthesis and materials preparation. $NFPI_7$ precursor solutions were prepared by dissolving NMAI, FAI and PbI_2 with a molar ratio of 2:1:2 in DMF (10 wt%) and stirred at 60 °C for 2 h in a nitrogen-filled glovebox. The NMAI was synthesized by adding 4.34 g hydroiodic acid (45 wt% in water) to a stirring solution of 1-naphthalenemethylamine (12.72 mmol) in tetrahydrofuran (THF, 50 ml) at 0 °C for 2 h. The solution was then evaporated at 50 °C to obtain the NMAI precipitate, which was washed three times with a $THF:CH_2Cl_2$ (3:1) mixture and then dried under vacuum. NMABr was synthesized by using similar method with the hydroiodic acid substituted by the hydrobromic acid. $NFPI_yB_{7-y}$ precursor solutions were prepared by altering composition of NMAI (NMABr), FAI (FABr) and PbI_2 ($PbBr_2$) with a molar ratio of 2:1:2 in DMF (10 wt%), except for $NFPI_2B_5$ from a precursor solution with a molar ratio of 2:1:1:1 in DMF (10 wt%) of $NMABr:FABr:PbBr_2:PbI_2$.

$(NMA)_2PbI_4$ precursor solutions were prepared by dissolving NMAI and PbI_2 with molar ratio of 1:1 in DMF (10 wt%) and stirred at 60 °C for 2 h in a glovebox.

Colloidal ZnO nanocrystals were synthesized by a solution–precipitation process and the details can be found in the literature[9].

Device fabrication. Solutions of ZnO nanocrystals were spin-coated onto the ITO-coated glass substrates at 4,000 rpm for 45 s and annealed in air at 150 °C. Then the substrates were transfered into a glovebox. Next, a solution of PEIE in 2-methoxyethanol (0.4 wt%) was spin-coated onto the ZnO films at a speed of 5,000 rpm. The substrates were rinsed twice with DMF, leaving ultrathin layers of PEIE on top of the ZnO films. The ultrathin layer of PEIE can significantly decrease the work function of ZnO[27]. The perovskite films were prepared by spin-coating the precursor solution onto the PEIE treated ZnO films, followed by annealing on a hot plate at 100 °C. The TFB layers were deposited from an *m*-xylene solution (8 mg ml^{-1}) at 2,000 rpm. Finally, the MoO_x/Au electrode was deposited using a thermal evaporation system through a shadow mask under a base pressure of ~6×10^{-7} torr. The device area was 3 mm^2 as defined by the overlapping area of the ITO films and top electrodes.

Characterization. All perovskite LED device characterizations were carried out at room temperature in a nitrogen-filled glovebox. A Keithley 2400 source meter and a fibre integration sphere (FOIS-1) coupled with a QE65 Pro spectrometer was used for the measurements[28]. The LED devices are tested on top of the integration sphere and only forward light emission can be collected, which is consistent with the standard OLED characterization method[29]. Supplementary Figure 9 shows the layout of our device characterization set-up. The devices were swept from zero bias to forward bias. The time evolution of the EQEs and voltages were measured using the same testing system. The angular dependence of emission intensity was measured by using a Thorlabs PDA100A detector at a fixed distance of 200 mm from the EL device. To verify the accuracy of the measurement set-up, we have cross-checked the performance of two sets of perovskite LEDs prepared under identical

conditions but measured separately at Nanjing Tech University and the University of Cambridge. The results obtained in the two different labs are in good agreement.

AFM images were collected in non-contact mode (Park XE7). The STEM images and EDX elemental mapping of the perovskite films were made on a FEI Titan G2 80–200 ChemiSTEM operated at 200 keV. Element determinations with outstanding sensitivity can be provided by ChemiSTEM EDX system. The HRTEM images were collected on a Tecnai G2 F20 microscope operated at 200 keV. The cross-sectional samples were prepared by using duel beam focused-ion-beam equipment (FEI Quata 3D FEG).

Ultraviolet–visible absorbance spectra were recorded on an ultraviolet–visible spectrophotometer with an integrating sphere (Cary 5000, Agilent). PL spectra of the perovskite films were measured at room temperature using a fluorescent spectrophotometer (F-4600, HITACHI) with a 200 W Xe lamp as an excitation source. The excitation spectra and time-resolved fluorescence spectra of the perovskite films were obtained by using an Edinburgh Instruments (FLS920) spectrometer. For the time-resolved PL measurements, the perovskite films were excited from the quartz glass substrate side by a 405 nm pulsed diode laser (EPL-405) with a fluence of around 4 nJ cm^{-2}. A three-step technique was used to obtain the PLQE of perovskite films by combination of a 445 nm Ccontinuous wave laser, optical fibre, spectrometer and integrating sphere[30].

For transient absorption measurements, the laser source was a Coherent LibraTM regenerative amplifier (50 fs, 1 KHz, 800 nm) seeded by a Coherent VitesseTM oscillator (50 fs, 80 MHz). 800 nm wavelength laser pulses were from the regenerative amplifier while 400 nm wavelength laser pulses were obtained with a barium boron oxide doubling crystal. Broadband femtosecond transient absorption spectra of the perovskite films were taken using the Ultrafast System HELIOSTM transient absorption spectrometer. The broadband probe pulses (420–800 nm) were generated by focusing a small portion (around 10 μJ) of the fundamental 800 nm laser pulses into a 2 mm sapphire plate. The thickness of the perovskite films is about 30 nm (same as in EL devices) for the above optical characterizations.

UPS spectra were collected on a Thermo ESCALAB-250Xi spectrometer with an applied bias of −10 V. He I ultraviolet radiation source (21.2 eV) was used. The overall resolution of the instrument is 0.1 eV.

References

27. Zhou, Y. *et al.* A universal method to produce low–work function electrodes for organic electronics. *Science* **336**, 327–332 (2012).
28. Dai, X. *et al.* Solution-processed, high-performance light-emitting diodes based on quantum dots. *Nature* **515**, 96–99 (2014).
29. Forrest, S. R., Bradley, D. D. C. & Thompson, M. E. Measuring the efficiency of organic light-emitting devices. *Adv. Mater.* **15**, 1043–1048 (2003).
30. De Mello, J. C., Wittmann, H. F. & Friend, R. H. An improved experimental determination of external photoluminescence quantum efficiency. *Adv. Mater.* **9**, 230–232 (1997).